Electrical and electrochemical studies of core–shell structured nanorods of LiMn$_2$O$_4$@PANI composite

K. F. Qasim[1,*] , W. A. Bayoumy[2], and M. A. Mousa[2]

[1] Chemistry Department, Faculty of Science, Menoufia University, Shibīn al-Kawm, Egypt
[2] Chemistry Department, Faculty of Science, Banha University, Banha, Egypt

ABSTRACT

Polyaniline has received much concentration in both basic and applied studies because it has electrical and electrochemical properties comparable to those of both conventional semiconductors and metals. In this work, PANI was used as a conducting additive to formulate a nanocomposite as a high functioning cathode material for Li-ion batteries. PANI, spinel cathode materials of LiMn$_2$O$_4$, and LMO@PANI were synthesized and characterized via scanning electron microscopy (SEM), Fourier transforms infrared spectroscopy (FT-IR), X-ray powder diffraction (XRD), and X-ray photoelectron spectroscopy (XPS). SEM of the composite illustrated the formation of long rods of LiMn$_2$O$_4$ covered by PANI layers. The electrical and electrochemical properties of the prepared materials were studied by electrochemical impedance spectroscopy as well as cyclic voltammetry. The composite sample showed higher electrical conductivity (5.5×10^{-2} S/cm) compared with that of PANI (9.1×10^{-4} S/cm) and also showed improving in its specific electrical capacity with a value of 75 mAh/g at a scan rate of 5 mV/s in 1 M LiNO$_3$ electrolyte compared with that of PANI (33 mAh/g). The cycling stability of the composite electrode was significantly improved and showed cycling performance, with ∼ 86.2% capacity retained over 1000 cycles. Results predict that the developed LMO@PANI nanocomposite could be used in an electrochemical energy storage device.

1 Introduction

Nowadays, high-power and high-energy rechargeable batteries and supercapacitors are very important devices for mobile and stationary energy storage applications [1]. Among the various energy storage systems, rechargeable lithium-ion batteries consider as one of the most promising energy sources in the electric vehicle due to their high working voltages, high energy density, long life, etc. [2]. LiMn$_2$O$_4$ (LMO) with spinel structure has become a popular cathode material in energy storage devices due to its ability to intercalate or de-intercalate Li-ions [3]. This is because it has reversible lithium intercalation, low price, high thermal and chemical stability, low

Address correspondence to E-mail: khaled_faisal92@hotmail.com

toxicity, natural abundance and capability of large scale production [4, 5].

Great steps have been taken in energy storage field and especially Li-ion batteries (LIBs) for either portable electronic devices or even heavy electric vehicles (EVs) as a cheap and eco-substitute of gasoline engines. EVs intensive research projects for EVs' batteries try to enhance durability, thermal stability, energy, and power density, cost, ionic, electronic transport resistance decrement, and bi-products of cathode materials as $LiCoO_2$, $LiMn_2O_4$, and $LiFePO_4$ [2].

In the $LiMn_2O_4$ cubic spinel structure (space-group:Fd3m), exhibits an array of O^{2-} occupy the 32 positions, Li^+ ions occupy 1/8 of the tetrahedral voids on the 8a site, and Mn^{3+}/Mn^{4+} ions occupy 1/2 of the octahedral voids on the 16d site. The Jahn–Teller distortion of Mn^{3+} is compensated by the statistical distribution of Mn^{3+}, and Mn^{4+} cations [6]. The electrode performance, in general, is highly influenced by the physico-chemical properties involving compositional stoichiometry, particle size, particle morphology, surface area, and crystallinity of the active material [7]. One of the considerable disadvantages of the LMO is the growth in Mn^{3+} ions content during lithium intercalation at low potentials ($\sim$ 3 V). Upon cycling, these ions produce a considerable variation in unit cell volume due to the Jahn–Teller effect which causes a break in the inter-particle contacts [8]. Moreover, the manganese dissolution throughout the electrochemical reaction and the kinetic topics connected to the low electronic conductivity and Li^+ diffusion coefficient and the quick capacity fading all through the cycling of spinel LMO limit their reasonable application in high power LIBs. To overcome the Mn dissolution, a lot of researchers are doing remarkable attempts to acquire stable LMO by using numerous approaches, comprising electrolyte additives and surface coating approach. Recent research established the significance of surface structural characters of electrode materials for their electrochemical performance so, an effective policy, coating the spinel $LiMn_2O_4$ with organic and inorganic compounds, has been investigated [9]. Numerous responsibilities for the coating approach have been proposed, comprising: (i) electrical conduction medium that assists the electron transport between the cathode active particles [10]. (ii) Modification of the cathode surface chemistry which varies chemical properties of the cathode surface to develop

stability and performance [11]. (iii) Physical protection barrier that suppresses electrolyte oxidation and cathode corrosion [12–16].

Between all known cathode materials for LIBs, $LiMn_2O_4$ is a suitable promising material for EVs cathodes, due to its availability, low price, eco-friendly properties, and capability of large scale production for EVs batteries manufacturing [2–4], but its capacity fades at 60 °C in acidic species liquid electrolyte [6–8]. So many attempts have been done to improve the performance of LMO by introducing dopants like Ni–Co–Mn [2, 17], Co–Mg–Ni [18], Ni [19], and S-doped [20], or coating LMO's surface with metal oxides like Al_2O_3 [9, 21], SiO_2 [10], ZrO_2 [11, 12], or salts like AlF_3 [13], $AlPO_4$ [14], or even polymer [15], or doping and coating like Ni–Co–Mn doping with Li_2ZrO_3 coating [17] as a protective layer for LMO direct exposure to electrolyte.

The coating layer's thickness should be controlled because if it was thick, it would work as a resistive layer, that leads to failing the electrochemical performance [22, 23].

LMO coated with $LiNi_{0.5}Mn_{1.5}O_4$ [24, 25], $LiCoO_2$ [26], and $Li_4Ti_5O_{12}$ [27], showing some problems at a higher temperature, although it shows high performance at room temperature.

The coating materials must also permit acceptable electrical and lithium transportation if they cover all the surface of each particle. Moreover, several coating properties may improve one aspect of performance while hindering another [24]. Several coating materials with variable characters and conventionality have been found to increase cathode performance as measured by both increasing the capacity and capacity retention [28].

LMO can be prepared by different methods, like conventional solid-state reaction [29], sol–gel [30], solid-state coordination reaction [31], microwave [32], and agitation [33].

Conducting polymers such as polyacetylene (PA) [34], polypyrrole (PPy) [35], polyaniline (PANI) [36], poly(3,4-ethylene dioxythiophene) (PEDOT) [15], etc. have attracted a significant consideration for their potential applications in different fields, such as corrosion protection coatings, rechargeable batteries [37], microwave absorption [38], electromagnetic interference (EMI) shielding [39], as well as electrodes and sensors. Recently, conducting polymer coating has been regarded as an economic and feasible technique to improve electrode performance.

Polyaniline as one kind of conducting polymers has drawn much interest among researchers for covering electrodes used in battery and supercapacitor devices [40]. This is because of its low cost, ease of preparation, stability, high conductivity, and robust mechanical properties such as flexibility and stretch-ability [38]. To enhance the efficiency of the electrodes used in energy systems, design, structure, composition, and fabrication techniques used for PANI and related composite have been focused on [41].

Based on the merits mentioned above, we prepared LMO@PANI binary composite material and compares its electrical and electrochemical properties with its constituents to investigate its ability to be used in electrochemical devices.

2 Experimental

2.1 Preparation of materials

2.1.1 Preparation of $LiMn_2O_4$ (LMO)

The traditional preparation method of the solid-state reaction was used for synthesizing $LiMn_2O_4$ with some modifications [42]. Li_2CO_3 and MnO_2 in two different molar ratios of 1:1.89 and 1:2 (Li/Mn) were mixed by dry ball-milling for 1 day, followed by heating the mixed powders at 800 °C for 2 h in air atmosphere. The samples were denoted as LMO (1) and LMO (2) for the samples with the molar compositions of Li:Mn equal to 1:1.89 and 1:2, respectively.

2.1.2 Preparation of polyaniline (PANI)

PANI was prepared by chemical polymerization [43]. 3 ml of aniline was mixed with 100 ml of 1 M of HCl to get aniline hydrochloride salt. 100 ml of 0.05 M $K_2S_2O_8$ used as an oxidant was titrated with aniline monomer for 4 h under stirring in an ice bath. The powder obtained was kept in the solution for a day before filtrating and washing with distilled water and methanol. Eventually, the resultant green powder was dried at 45 °C for 24 h.

2.1.3 Preparation LMO@PANI composite

PANI@LMO composite was synthesized by using aniline monomer and LMO (1) in a weight ratio of LMO (1): aniline monomer is 1:1 by a similar method to that mentioned above for preparing PANI.

2.2 Materials characterizations and measurements

X-ray diffraction (XRD) was measured using X-Pert diffractometer with Kα- Cu source λ = 154 pm. The analysis was recorded for 2θ in the range 15°–80°. Fourier transform Infrared spectroscopy (FT-IR) spectra were recorded in the range of 4000–400 cm^{-1} using (Thermo Scientific Nicolet iS10). The prepared samples were also analysed by scan electron microscopy (SEM) using (JEOL JEM-100CXII), and transmission electron microscopy (TEM) using JEOL-2010 techniques. X-ray photoelectron spectroscopy (XPS) was performed using a KRATOS XSAM-800 for composite sample in range 0–1200 eV.

2.3 Electrochemical and electric measurements

2.3.1 Preparation of working electrodes

Electrodes were prepared by coating a paste formed from investigated materials, acetylene black and polyvinylidene fluoride with mass ratio 75:15:10, respectively, with ethanol as a solvent on FTO and dried at 80 °C for 2 h.

Electrochemical behaviors were studied by Galvanostatic charge–discharge (GCD) and cyclic voltammetry (CV) using a potentiostat (Digi-Ivy 2116, USA). Electrochemical impedance spectroscopy (EIS) were measured on a (Metrohm autolab PGSTAT 204, Netherlands) at constant potential 10 mV and frequency ranged from 0.1 Hz to 100 kHz. The electrochemical studies were carried out in three-electrode cell with the prepared active material coated on FTO glass works as a working electrode, sheet Pt (2 cm^2) and saturated calomel electrode, as a counter, and a reference electrode, respectively. The CV was performed between −1 and 1.2 V at a scan rate 10 mV/s. GCD was measured at a current density 1 A/g. All measurements were taken in 1 M $LiNO_3$ aqueous electrolyte solution.

The electrical measurements were taken at a constant voltage (1 V), in a frequency ranging between 10^3 and 10^7 Hz at 25 °C, using a programmable automatic LCR bridge (GW Instek 8110G LCR meter, Taiwan). The complex dielectric permittivity was investigated using the relation [44]

$$\varepsilon * (\omega) = \varepsilon''(\omega) \, - \, \mathrm{j}\varepsilon''(\omega) \tag{1}$$

(ε' is the real part of the permittivity, ε'' is the imaginary part of the permittivity with $j = \sqrt{-1}$). The dielectric constant was calculated from the equivalent capacitance (C). The loss factor (tan δ) was recorded at a given frequency. The values for ε' and ε'' were estimated using Eqs. (2), (3) [44]

$$\varepsilon' = \frac{Cd}{\varepsilon^o A_s} \tag{2}$$

$$\varepsilon''(\omega) = \varepsilon'(\omega)\tan\delta \tag{3}$$

where ε^o is the permittivity of the vacuum, d is thickness, A_s is the cross-sectional area of the specimen, tan δ is a dissipative factor, and δ-phase angle, with $\omega = 2\pi f$, f is the frequency of the applied electric field.

The sheet resistivity (R_s) of the different samples was measured at room temperature by using a four-point probe system (RTS-9 4 PROBES TECH Guangzhou, China). Each sample was tested 5 times at different positions of the sample, and the average of all the measurements was taken. The electrical resistivity (ρ) of the sample was then calculated according to the equation: $\rho = R_s \, d$, where d is the thickness of the film.

3 Results and discussion

3.1 Characterizations

The XRD patterns of LMO samples obtained using two different stoichiometric ratios are shown in Fig. 1a. The XRD patterns of LMO (2) sample with the molar ratio of 1:2 (Li:Mn) showed the formation of LMO cubic spinel phase structure as a major product with diffraction peaks at 18°, 36°, 38°, 44°,48°, 58°, 64°, 68°, 75°, and 77° referring to (111), (311), (222), (400), (331), (511), (440), (531), (533), and (622) planes, respectively, (JCPDS card no. 35-0782) [10]. Besides the major peaks, some impurity phases corresponding to α-Mn_2O_3 at 33.5° referring to (110) plane (JCPDS card no. 41-1442) are observed, which denotes that not all amounts of MnO_2 reacted with Li_2CO_3. Therefore another sample (LMO (1)) under the same conditions was prepared with a stoichiometric ratio of 1:1.89 Li:Mn.

The XRD of the LMO (1) sample clarified the formation of the pure cubic spinel phase of $LiMn_2O_4$ with an (Fd3m) space group. The lattice constant (a) of the second sample is evaluated by Eq. (4)

$$d_{hkl} = a/\sqrt{\left(h^2 + k^2 + l^2\right)} \tag{4}$$

where (hkl) are the Miller indices and found to be 8.21 Å.

The XRD of PANI and LMO@PANI samples are represented in Fig. 1b. PANI showed a broad peak at $2\theta = 25.5°$ indicating an amorphous structure for the sample. Whereas, the XRD of PANI@LMO sample showed beside the amorphous peak (at $2\theta = 25.5°$) three characteristics peaks for Mn_5O_8 at $2\theta = 29.5°$, 31.2° and 43.5° related to (111), (310), and (112) plans, respectively (JCPDS No. 39-1218) due to de-lithiation (Li-ion migration from LMO), in addition to three peaks at almost the same locations 18.3°, 38.2°, and 64.4° characteristic for the formation of Li_2MnO_3 (JCPDS No. 39-1218) and $LiMn_2O_4$ [45, 46]. The XRD pattern peaks of the composite sample show a slight movement towards the smaller angle, which indirectly interprets the increase of the unit cell volume of the composite sample. These results indicated that PANI and LMO (1) were to some extent interacted, and LMO@PANI composite is obtained according to the following chemical equation.
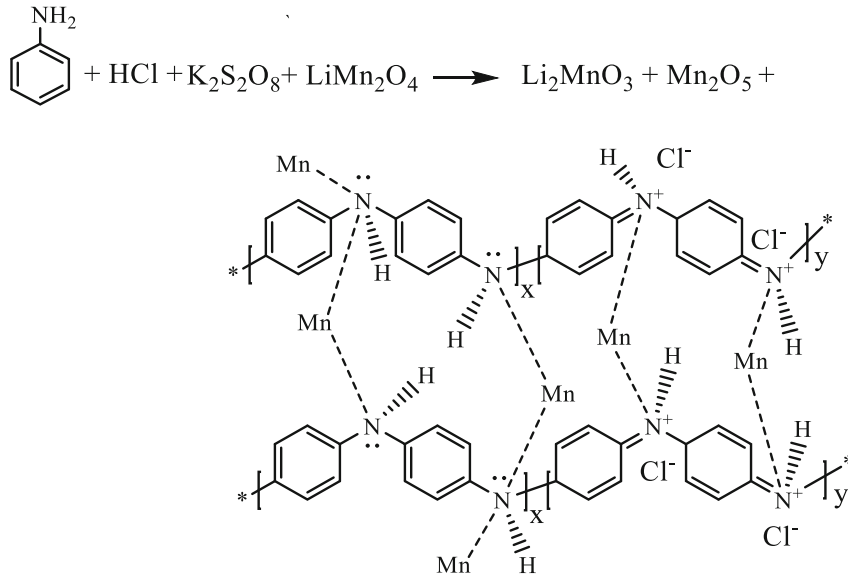
Fig. 1 XRD of **a** LMO samples, and **b** PANI & LMO@PANI
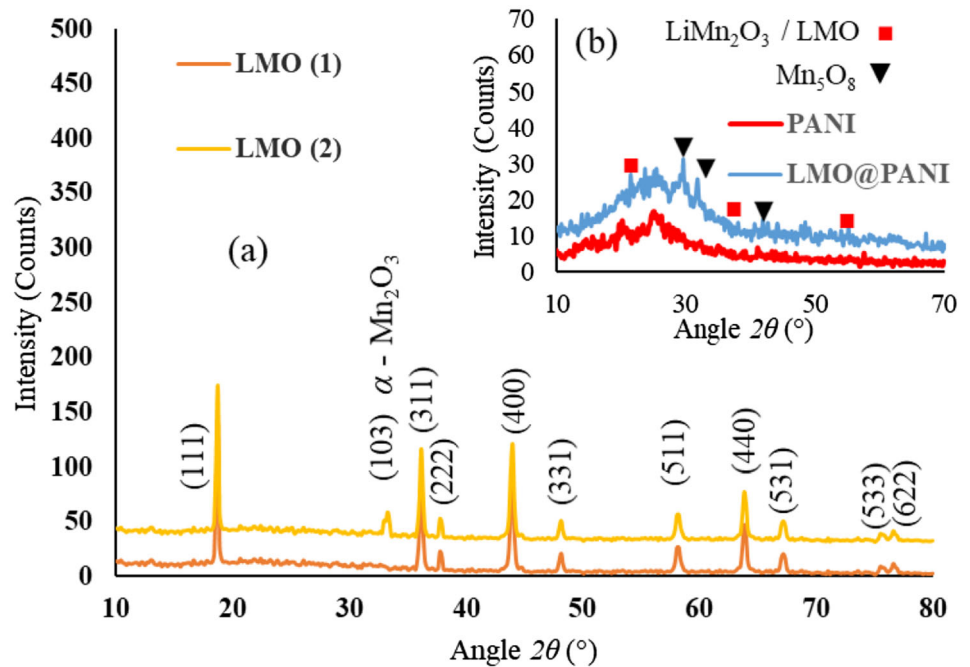
To understand the impact of the addition of PANI into LMO (1) crystals, the crystallite size and the strains obtained in the crystals are calculated from XRD data. The mean crystalline structure was calculated by Debye–Scherrer's Eq. (5) [47], and the strain (ε) by Eq. (6) [47].

$$D = \frac{0.9\lambda}{\beta\cos\theta} \quad (5)$$

$$\varepsilon = \frac{\beta}{4\tan\theta} \quad (6)$$

where λ is the X-ray wavelength used and β is the half peak width of the diffraction peak. The results obtained are listed in Table 1. The enlarge in each of crystal size, unit volume and the strain of LMO crystal due to the addition of PANI chains can be caused by the relaxation of strain [48]. This will reduce the one-electron bandwidth, which will

Table 1 XRD and electrochemical capacitive data of the investigated materials

Sample	C_{sp} (mAh/g)	Crystal size (nm)	ε	E (W/kg)	P (W/kg)	Efficiency after 1000 cycles (%)	R_S (Ω)	R_{ct} (Ω)
LMO (1)	35 (21)	62	9.7×10^{-3}	20	443	84.3	20	81
PANI	33 (26)	–	–	50.2	2200	81.8	58	16
LMO@PANI	75 (70)	–	1×10^{-2}	46.3	1090	86.2	28	21

() is C_{sp} from GCD
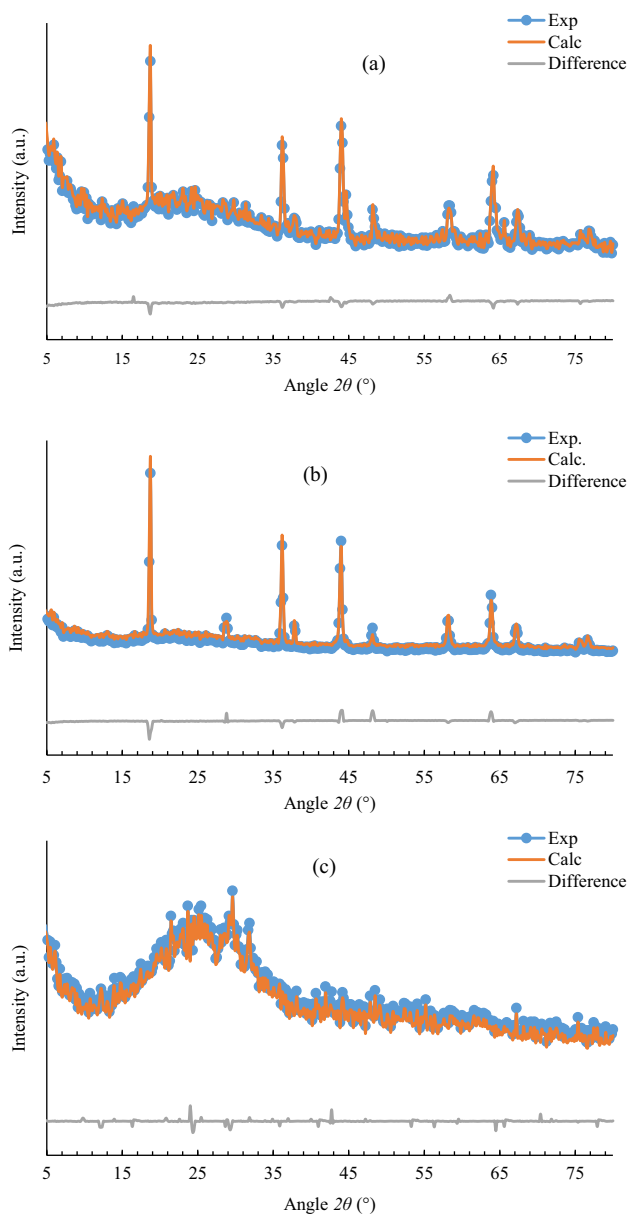
**Fig. 2** Rietveld refinement method for **a** LMO (1), **b** LMO (2), and **c** LMO@PANI

weaken the overlap between O $2p$ and Mn $3d$ orbital, thus favors the charge localization [49]. These results reveal that PANI is not only formed on the surface of LMO, but it can be also introduced inside the crystals [45].

To clarify the qualification and quantification of the phases formed in LMO and LMO@PANI composite samples, a mathematical Rietveld method was applied. The obtained results, which grounded on a model of Li1 atoms occupying the 8a (1/8, 1/8, 1/8) location, Li2/Mn atoms occupying the 16d (1/2, 1/2, 1/2) location, and O atoms occupying the 32e (x, x, x), are presented in Fig. 2, and listed in Table 2. Some significant changes in structure were found between the LMO (1) and LMO (2) samples. The LMO (2) sample with a molar ratio of Li:Mn = 1:2 showed a presence of α-Mn$_2$O$_3$ phase with 1.12 wt%, and exhibit larger lattice parameter (a), lattice volume (V), oxygen coordinate (x'), and Mn–O bond distance. The goodness of fit (low R_p, R_{wp}, and R_{exp} values, as shown in Table 2 confirm the refinement process. The smaller value of x' suggested decreasing structural distortion [50], and the increase in the lattice parameter value indicate the presence of a higher amount of Mn^{3+} ions than the Mn^{4+} ions in the spinel structure. Moreover, it reveals a low amount of cation vacancies and resemblance in cation distribution between the tetrahedral and octahedral site [46]. One possible source of the differences in unit cells of the studied samples could be attributed to the variation in the number of oxygen vacancies. A presence of higher concentration of oxygen vacancies in the structure leads to a reduction in the average oxidation state of Mn, and consequently raises the ionic radius and expands the unit cell.

Figure 3 presents FT-IR diagrams of LMO (1), PANI, and LMO@PANI. FT-IR of LMO (1) has 2 bands at 632 and 584 cm^{-1} referring to Li–O, and Mn–O vibrations, respectively, characterizing for spinel structure of LMO (1) [3]. FT-IR of PANI

Table 2 Rietveld mathematical data of the LMO (1), LMO (2) and LMO@PANI samples

Sample	a (Å)	V (Å³)	x'	Mn–O (Å)	α-Mn₂O₃ (wt%)	Mn₅O₈ (wt%)	R_p (%)	R_{wp} (%)	χ^2
LMO (1)	8.2478	561.06	0.2551	1.957	–	–	4.99	6.61	2.612
LMO (2)	8.2601	563.57	0.2583	1.971	1.12	–	5.32	7.59	3.134
LMO@PANI	8.2547	562.48	0.2578	1.964	–	2.7	6.57	7.83	3.19
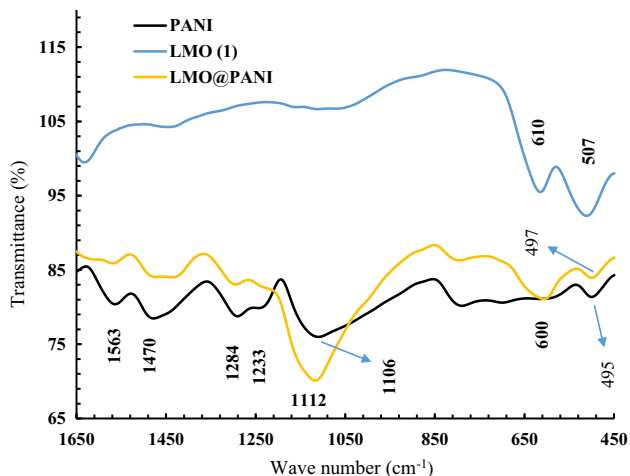
Fig. 3 FT-IR of the investigated materials
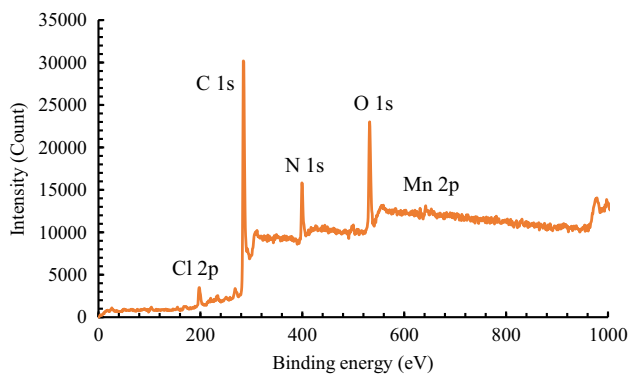
Fig. 4 XPS of LMO@PANI

showed vibration bands at 1561 and 1471 cm^{-1} related to the C=C and C=N stretching bands of the quinoid and benzenoid rings, respectively, that refers to formation of (Pernigraniline, PRG) or the oxidized form of PANI. Moreover, the bands observed at 1284, and 1233 cm^{-1} are related to N–H bending and asymmetric C–N stretching modes of benzenoid ring, respectively, which prove the presence of a reduced form of PANI (emeraldine salt, ES) and indicate that PANI has the half-reduced form (leuco-emeraldine salt, LES). FT-IR of PANI also showed a band at ∼ 1108 cm^{-1}, which is associated with bending

vibrational modes of quinonic-type rings [51] referring to the polymerization of aniline.

The spectrum of LMO@PANI sample showed shifts in the absorption peaks of PANI and LMO samples, especially for 1112 cm^{-1} of C–N bending, and 600 cm^{-1} of Mn–N vibration. That demonstrates the successful interaction between LMO and PANI.

Figure 4 demonstrates the X-ray photoelectron spectroscopy (XPS) scan of LMO@PANI composite sample in binding energy (B.E.) ranges from 0 to 1200 eV. The spectrum shows that the LMO@PANI sample contains main elements: Cl, O, C, Mn, and N suggesting the formation of the composites and the elemental analysis of Mn, C, N, O, and Cl were found to be 2.49, 69.55, 9.75, 14.81, and 3.39 wt%, respectively.
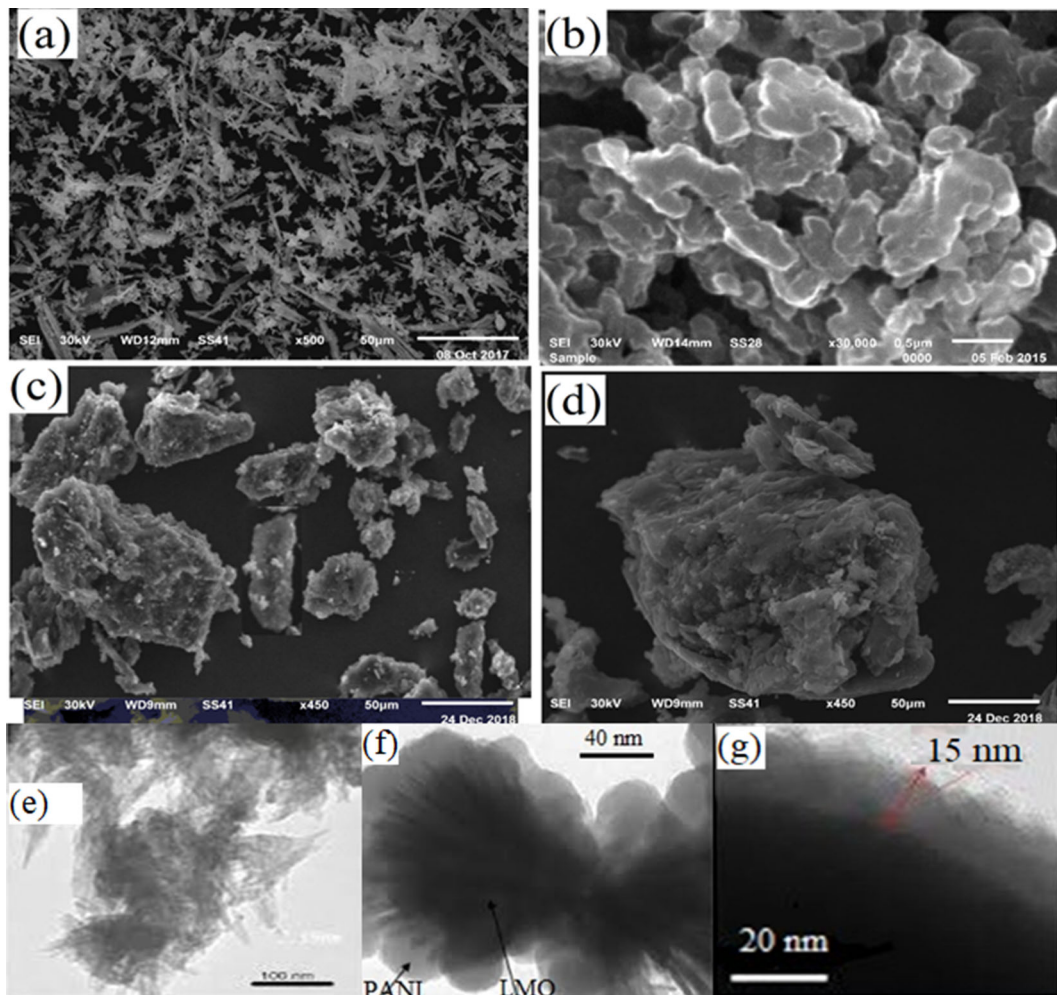
SEM of LMO (1), PANI, and LMO@PANI are presented in Fig. 5a–c. SEM of LMO (Fig. 5a) displays smooth rod morphology with average length of 0.16 μm, whereas SEM image of PANI (Fig. 5b) illustrates clusters of sheets morphology with an average grain size of 0.8 μm. SEM of LMO@PANI (Fig. 5c) shows a core–shell structure of LMO (1) with the polymer base shell, and form agglomerates of size 75 μm, which in turn results in the distribution of LMO (1) in PANI. The images obtained (Fig. 5d, e) show the formation of LMO (1) rods covered by PANI layer with a thickness of ∼ 15 nm.

3.2 Electrical studies

To get knowledge on the type of polarization state in the studied samples, the ac-electrical measurements in room temperature and at a frequency range of 10^3–10^7 Hz were investigated. The ac-conductivity (σ_{ac}) was evaluated using Eq. (7) [44]

$$\sigma_{ac} = \frac{t V_r \cos(\frac{\varnothing}{\pi} \times 180)}{RA} \qquad (7)$$

where t is thickness, V_r is potential, ϕ is the phase angle, R is the resistance used and A is the cross-section area. The frequency dependence of the ac-

Fig. 5 SEM of **a** LMO (1), **b** PANI, **c** LMO@PANI, **d** LMO@PANI (magnified view), **e**–**g** TEM images of (LMO@PANI)

conductivity (σ_{AC}) of LMO (1), PANI, and their composite are illustrated in Fig. 6a. For all samples, σ_{AC} is nearly steady until frequency $\sim$ 500 kHz, followed by a sudden rise at higher frequencies, where the ac-conductivity at all applied frequencies increases in the order: LMO@PANI > PANI > LMO (1), as listed in Table 3. This could be attributed to the presence of interfacial phases which increases the polarization in the samples.

The cole–cole diagrams of the electrical impedance (EIS) data of the studied samples were represented in Fig. 6b. The plot of each sample shows an almost single depressed semi-circular shape passing near the origin point, which implies to a parallel grouping of grain boundary resistance and grain boundary capacitance. It is interesting to notice that the centre of each semi-circle is located near the real axis, i.e.,

the angle of dispersion is insignificant [52, 53]. It also refers to that LMO@PANI is electrically homogeneous. The EIS data for each sample are listed in in Table 3, which shows that the bulk resistance follows the order:

LMO (1) > > PANI > LMO@PANI.

Bulk conductivity was also measured by four probe method and found to be 7.04 × 10^{-5} S/cm, 1.46 × 10^{-3} S/cm, and 7.8 × 10^{-2} S/cm for LMO (1), PANI and LMO@PANI, respectively.

The conductivity depends on several external factors such as compactness, delocalized length and particles orientation. Thus, the higher conductivity of LMO@PANI composite than that of the polyaniline could be explained on the basis of the compactness of PANI on the LMO (1) surface (see strain result), more delocalization length and strong coupling through

**Fig. 6** Effect of frequency on **a** σ_{AC}, and **b** EI for the investigated materials
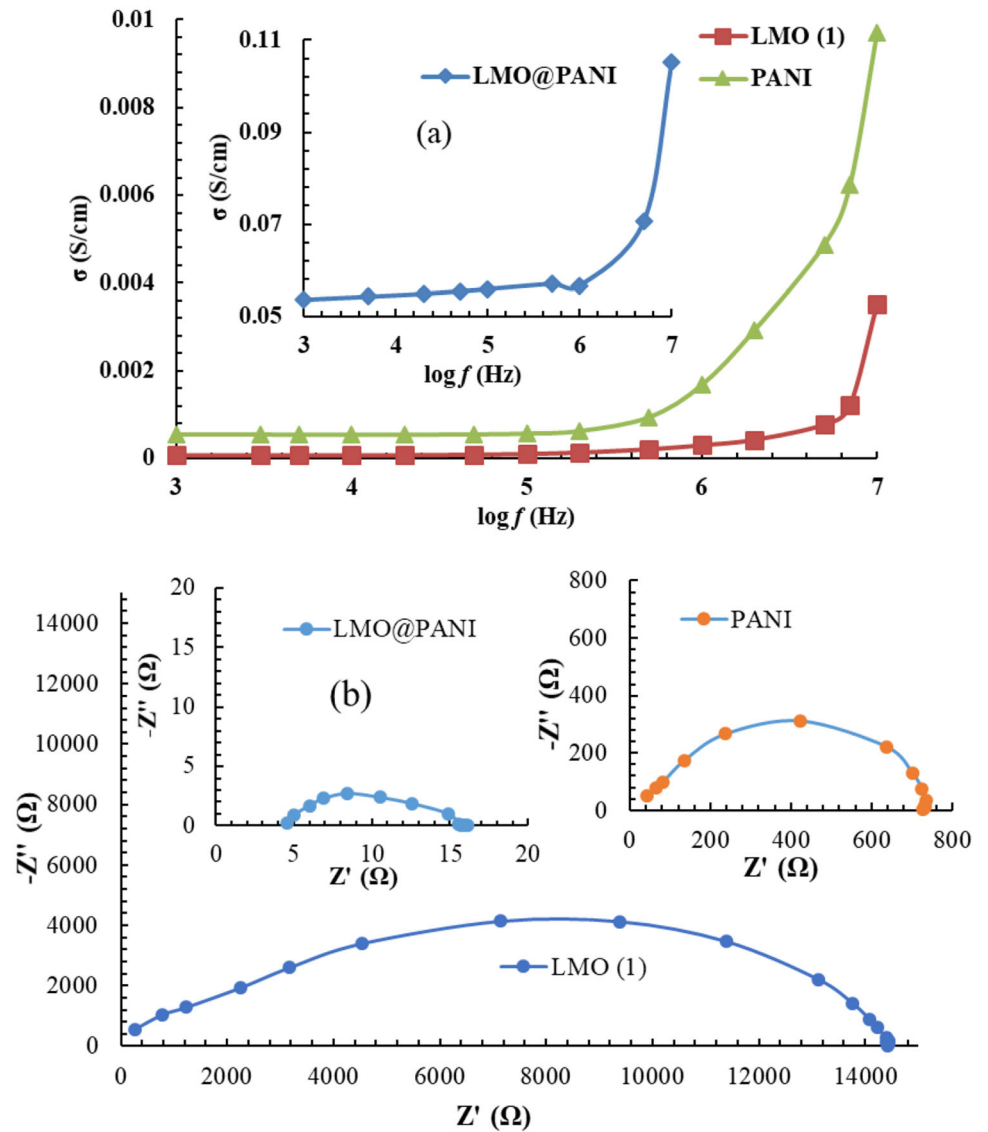
Table 3 Effect of frequency on dielectric data of the investigated materials

Sample	1000 Hz			500 kHz			10 MHz			R_b (Ω)
	σ (S/cm)	ε'	ε''	σ (S/cm)	ε'	ε''	σ (S/cm)	ε'	ε''	
LMO (1)	6.6×10^{-5}	6.2×10^4	3.0×10^6	1.1×10^{-4}	4.1×10^1	0.94×10^2	3.5×10^{-3}	0.31×10^1	0.14×10^1	14.2×10^3
PANI	8.1×10^{-4}	3.01×10^6	7.1×10^8	9.1×10^{-4}	4.6×10^1	6.21×10^1	9×10^{-3}	13.8	1.10×10^1	6.85×10^2
LMO@PANI	5.3×10^{-2}	2.11×10^9	6.4×10^{12}	5.5×10^{-2}	2.1×10^6	8.82×10^8	1.1×10^{-1}	3.0×10^2	4.96×10^2	14.4

the grain boundary. Moreover, the clear upgrading in the electrochemical functioning of the composite LMO@PANI over neat PANI and LMO (1) are

attributed to that the high conductive composite has a comparatively small diffusion path of the ions in the electrolyte, a reduce of the internal resistance and a
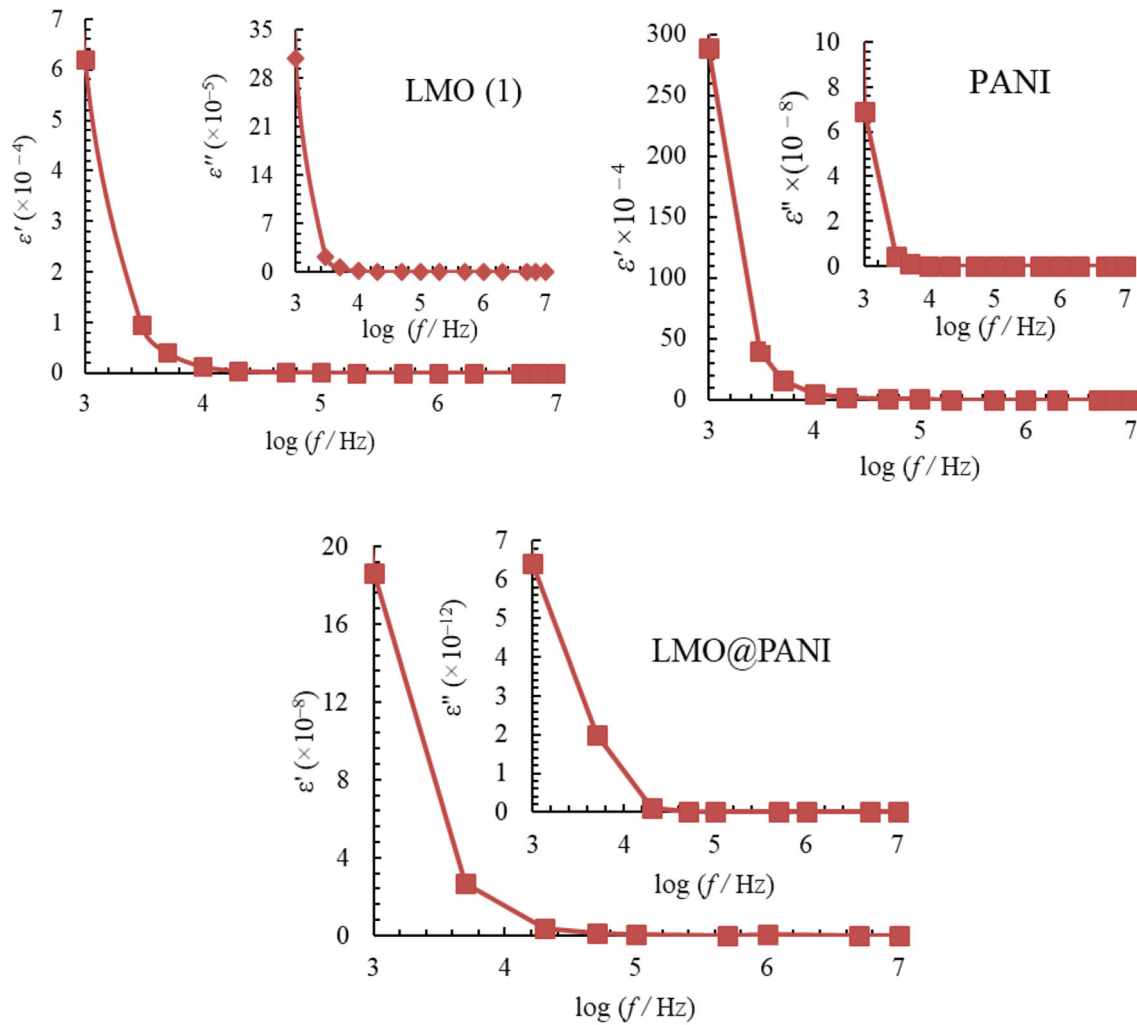
Fig. 7 Effect of frequency on ε', ε'' for investigated materials

rise of the electrolyte ion transport rate, which would donate to high capacity.

The frequency dependence of ε', and ε'' for the investigated materials are represented in Fig. 7. All samples show dielectric dispersion, where both ε', ε'' values reduce quickly with rising frequency in the low-frequency section and approach almost frequency self-regulating trend at higher frequencies. This can be obtained from the decrease in the polarization of the dipoles when the electric field propagates at higher frequencies [54]. This can be also attributed to the presence of a large number of interfaces in the nanomaterials with great volume fractions, which hold a huge number of defects that produces a variant in (+) and (−) space charge distribution at interfaces. By putting on the electric field, the space charges move and when they are trapped by defects, a big number of dipole moments are produced. At low-frequency section, these dipole moments are easy going to follow the alteration of electric field. Consequently, ε', and ε'' shows high value at low frequency as shown in our results.

3.3 Electrochemical measurements

Cyclic voltammetry (CV) is a proper method to observe capacitive mechanisms. Figure 8a shows the diagrams of CV for the investigated electrode materials at 10 mV/s in 1 M aqueous $LiNO_3$. LMO (1) and PANI display different electrochemical redox behavior, which is highly observed at higher scanning rates [55]. The CV plot of LMO (1) showed redox peaks at − 0.76 V, and − 0.45 V due to Li hopping inLMO (1) crystal structure as a result of mutual Li^+ intercalation in the electrolyte. PANI showed a couple of redox peaks at − 0.77 V, and − 0.45 V due to
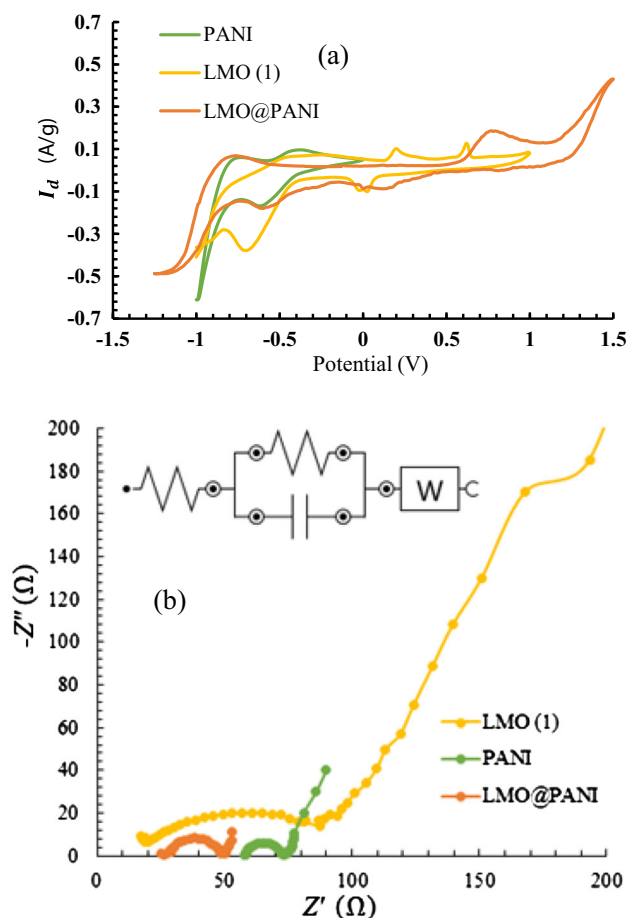
Fig. 8 **a** CV, and **b** EIS of the investigated materials

LES $\leftrightarrow$ ES $\leftrightarrow$ PRG transformations respectively [56]. Besides, reduction peaks appeared at -0.52 V and -0.65 V referring to PRG $\leftrightarrow$ ES $\leftrightarrow$ LES. The specific capacity (C_{sp}) was calculated from CV data according to Eq. (8) [57].

$$C_{sp} = \frac{1}{mv\Delta V} \int_{-V}^{+V} IV \partial V \tag{8}$$

where C_{sp} is specific capacity (mAh/g), I is current (A), V is applied potential (V), (v) is scan rate (V/s), and m is mass of active material (g).

The CV voltammogram of LMO@PANI composite (given in Fig. 8a) shows the presence of the identical earlier-stated peaks for PANI and LMO with varied shift ± 0.03 V, in addition to redox peaks at -0.06 V and 0.12 V referring to $Mn^{+3} \leftrightarrow Mn^{+2}$ and at 0.7 V referring to $Mn_2O_4^{-1} \leftrightarrow MnO_3^{-2}$ [58], which related to LMO (1), and PANI interaction occurring in composite structure. C_{sp} values acquired from CV are listed in Table 1.

To better understand the charge transfer kinetics, electrochemical impedance spectroscopy (EIS) measurement was performed. The Nyquist plots of investigated electrodes over a frequency range of 10^{-2} to 10^5 Hz are given in Fig. 8b. The three electrodes showed the same behavior with different values for the charge transfer resistance (R_{ct}) at the high-frequency region, which is linked with the surface character of the electrode and relating to the charge transfer resistance R_{ct} at the electrode/electrolyte interface. At the high-frequency section, the intersection ended of the semicircle with the Z'—axis shows the equivalent series resistance (ESR). The acquired impedance data are given in Table 1, which demonstrates that R_{CT} increases in the order of LMO (1) > PANI > LMO@PANI. This indicates that introducing PANI into LMO (1) material causes an increase in Li-ion conductivity that resulted in enhanced cycling performance [28]. The spike observed on the Nyquist plot for each electrode at the low-frequency section points to the distinguishing character of supercapacitors and positions of Warburg impedance of the electrode, i.e., the resistance of the diffusion of Li^+ and NO_3^- ions into the electrode.

Galvanostatic charging—discharging (GCD) is a corresponding method to determine C_{sp} of electrochemical storage systems at fixed current. Thus, the electrochemical presentations of studied electrodes were also examined using GCD. All GCD plots (Fig. 9a) displayed an internal resistance drop (IR-drop) knowing as the equivalent series resistance (ESR), which includes all the resistances of the cell (electrode, electrolyte, contact resistance) [56]. The specific capacity values C_{sp} of the electrodes were evaluated from the discharge cycles by using Eq. (9) [56, 59].

$$Csp = \frac{I\Delta t}{m\Delta V} \tag{9}$$

where I is the response current, Δt is the discharge time, ΔV is the potential range during the charge–discharge measurement and m is the mass of the active materials on the electrode. The results obtained are listed in Table 1. The specific capacity values obtained from the GCD technique are in good agreement with those obtained from CV measurements and found to be increased in the order LMO@PANI > PANI > LMO (1). This can be assigned to the synergistic effect produced from the individual materials.

Fig. 9 **a** GCD and **b** stability of the investigated materials
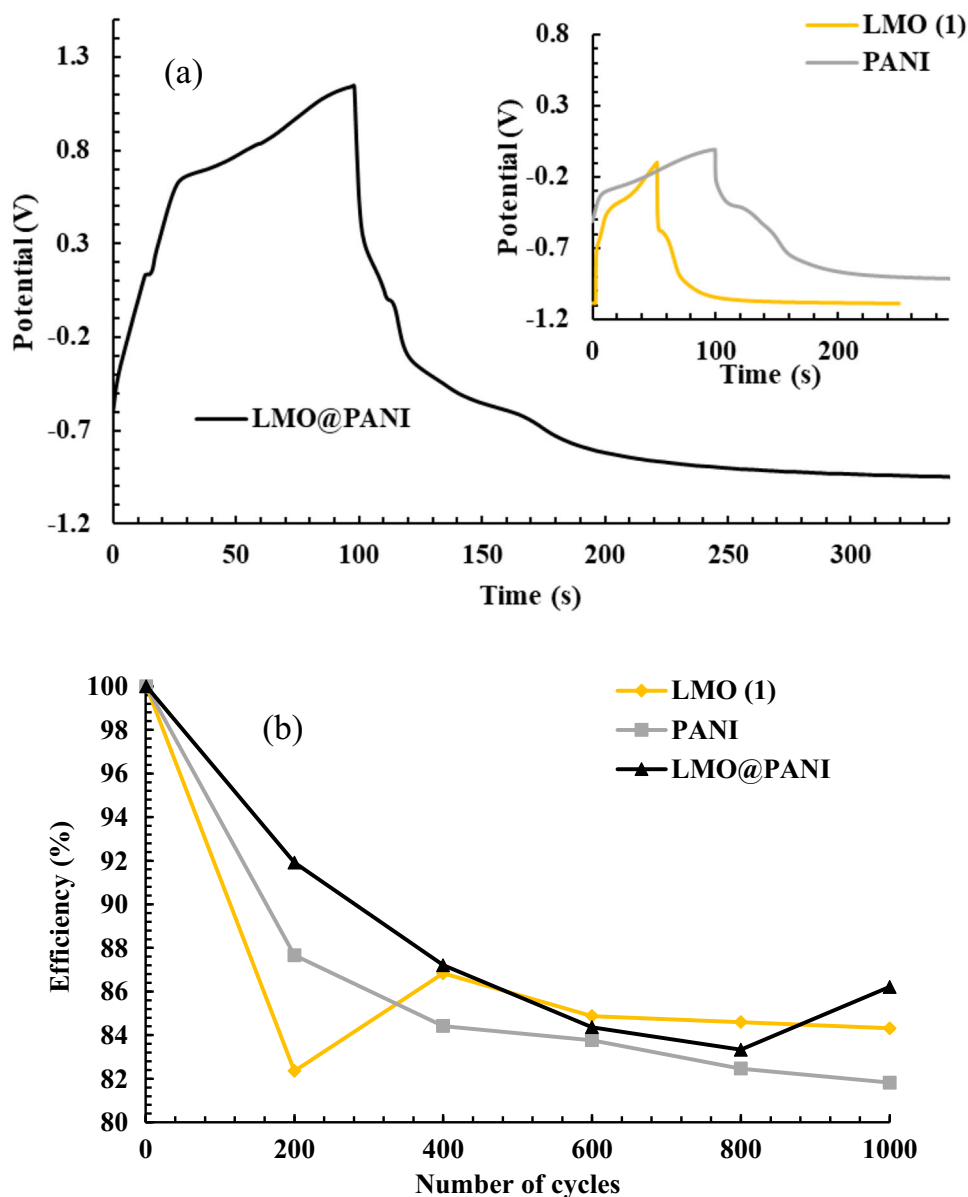
Cycling stability is a significant factor for energy storage uses. Therefore, it was examined for the investigated electrodes at current density of 1 A/g. The results are illustrated in Fig. 9b and listed in Table 1, which show that the binary electrode retained about 86.2% of its initial capacity after 1000 cycles and has widespread limit reversibility in successive charge/discharge cycles. The high stability of the binary system might be attached to the synergetic interaction among binary system components.

In general, the better electrochemical performance of LMO@PANI among all the synthesized samples can be attributed to the lower Jahn–Teller distortion effect that provides chemical and structural stabilization [4], more uniform and low agglomerated nanoparticles, low charge transfer resistance (as evident from EIS measurement) and possibly higher electronic conductivity provided by introducing PANI into LMO.

4 Conclusions

In conclusion, pure LMO (1) nanoparticles were successfully synthesized using a solid-state reaction method in the air atmosphere, while PANI was prepared by in situ polymerization. AC—electrical properties and electrochemical behaviours of LMO

(1), PANI, and their composite were investigated. The results showed that the PANI enhances the electrochemical and dielectric behaviours of LMO (1) and the specific capacity follows the order: LMO @PANI > PANI > LMO (1). And the stability of the composite electrode is higher than its individual constituent and exhibit 89% of its initial capacity after 1000 cycles. The better electrochemical performance of LMO@PANI among all the synthesized samples can be attributed to the lower Jahn–Teller distortion effect that provides chemical and structural stabilization, more uniform and low agglomerated nanoparticles, low charge transfer resistance (as evident from EIS measurement) and possibly higher electronic conductivity provided by introducing PANI into LMO (1). The obtained results show the possibility of using the developed LMO@PANI nanocomposite electrode in an electrochemical energy storage device.

Compliance with ethical standards

References

1. M. Li, J. Lu, Z. Chen, K. Amine, 30 years of lithium-ion batteries. Adv. Mater. **30**, 1–24 (2018)

2. N.S. Choi, Z. Chen, S.A. Freunberger et al., Challenges facing lithium batteries and electrical double-layer capacitors. Angew. Chem. Int. Ed. **51**, 9994–10024 (2012)

3. B. Dunn, B. Dunn, H. Kamath, J. Tarascon, Electrical energy storage for the gridfor the grid: a battery of choices. Science **334**, 928–936 (2011)

4. H.W. Lee, P. Muralidharan, R. Ruffo et al., Ultrathin spinel $LiMn_2O_4$ nanowires as high power cathode materials for Li-ion batteries. Nano Lett. **10**, 3852–3856 (2010)

5. M. Winter, B. Barnett, K. Xu, Before Li ion batteries. Chem. Rev. **118**, 11433–11456 (2018)

6. Z.H. Chen, J.L. Cao, W.A. Yan, S.U. Guang et al., Synthesis and characterization of ε-$VOPO_4$ nanosheets for secondary lithium-ion battery cathode. Trans. Nonferrous Met. Soc. China (English Ed) **27**, 377–381 (2017)

7. J.S. Kim, K. Kim, W. Cho et al., A truncated manganese spinel cathode for excellent power and lifetime in lithium-ion batteries. Nano Lett. **12**, 6358–6365 (2012)

8. Y. Xia, Capacity fading on cycling of 4 V Li/$LiMn_2O_4$ cells. J. Electrochem. Soc. **144**, 2593–2599 (1997)

9. J. Cho, Y.J. Kim, Enhanced structural stability of o-$LiMnO_2$ by sol-gel coating of Al_2O_3. Chem. Mater. **13**, 18–20 (2001)

10. D. Arumugam, G. Paruthimal Kalaignan, Synthesis and electrochemical characterizations of Nano-SiO_2-coated $LiMn_2O_4$ cathode materials for rechargeable lithium batteries. J. Electroanal. Chem. **624**, 197–204 (2008)

11. P.S. Bin, H.C. Shin, W.G. Lee et al., Improvement of capacity fading resistance of $LiMn_2O_4$ by amphoteric oxides. J. Power Sources **180**, 597–601 (2008)

12. S. Lim, J. Cho, PVP-Assisted ZrO_2 coating on $LiMn_2O_4$ spinel cathode nanoparticles prepared by MnO_2 nanowire templates. Electrochem. Commun. **10**, 1478–1481 (2008)

13. Y. Liu, J. Lv, Y. Fei et al., Improvement of storage performance of $LiMn_2O_4$/graphite battery with AlF_3-coated $LiMn_2O_4$. Ionics **19**, 1241–1246 (2013)

14. D. Liu, Z. He, X. Liu, Increased cycling stability of $AlPO_4$-coated $LiMn_2O_4$ for lithium ion batteries. Mater. Lett. **61**, 4703–4706 (2007)

15. C. Arbizzani, A. Balducci, M. Mastragostino et al., Characterization and electrochemical performance of Li-rich manganese oxide spinel/poly(3,4-ethylenedioxythiophene) as the positive electrode for lithium-ion batteries. J. Electroanal. Chem. **553**, 125–133 (2003)

16. S.C. Canobre, L. Montanhez, C.P. Fonseca, S. Neves, Development of composites based on lithium manganese nickel oxide and electroactive polymers. Mater. Chem. Phys. **114**, 350–355 (2009)

17. J. Ni, H. Zhou, J. Chen, X. Zhang, Improved electrochemical performance of layered $LiNi_{0.4}Co_{0.2}Mn_{0.4}O_2$ via Li_2ZrO_3 coating. Electrochim. Acta **53**, 3075–3083 (2008)

18. Y. Yu, M. Xiang, J. Guo et al., Enhancing high-rate and elevated-temperature properties of Ni–Mg co-doped $LiMn_2O_4$ cathodes for Li-ion batteries. J. Colloid Interface Sci. **555**, 64–71 (2019)

19. Y. Duan, J. Guo, M. Xiang et al., Single crystalline polyhedral $LiNi_xMn_{2-x}O_4$ as high-performance cathodes for ultralong cycling lithium-ion batteries. Solid State Ionics **326**, 100–109 (2018)

20. K. Chudzik, M. Lis, M. Świętosławski et al., Improving the performance of sulphur doped $LiMn_2O_4$ by carbon coating. J. Power Sources **434**, 226725 (2019)

21. S. Li, K. Zhu, D. Zhao et al., Porous $LiMn_2O_4$ with Al_2O_3 coating as high-performance positive materials. Ionics (Kiel) **25**, 1991–1998 (2019)

22. S. Lee, Y. Cho, H.K. Song et al., Carbon-coated single-crystal $LiMn_2O_4$ nanoparticle clusters as cathode material for high-energy and high-power lithium-ion batteries. Angew. Chem. – Int. Ed. **51**, 8748–8752 (2012)

23. M.-J. Lee, S. Lee, P. Oh et al., High performance $LiMn_2O_4$ cathode materials grown with epitaxial layered nanostructure for Li-ion batteries. Nano Lett. **14**, 993–999 (2014)

24. E.S. Lee, A. Huq, H.Y. Chang, A. Manthiram, High-voltage, high-energy layered-spinel composite cathodes with superior cycle life for lithium-ion batteries. Chem. Mater. **24**, 600–612 (2012)

25. S.T. Myung, K.S. Lee, D.W. Kim et al., Spherical core-shell $Li[(Li_{0.05}Mn_{0.95})_{0.8}(Ni_{0.25}Mn_{0.75})_{0.2}]_2O_4$ spinels as high performance cathodes for lithium batteries. Energy Environ. Sci. **4**, 935–939 (2011)

26. J. Cho, G.B. Kim, S. Lim et al., Improvement of structural stability of $LiMn_2O_4$ cathode material on 55°C cycling by sol-gel coating of $LiCoO_2$. Electrochem. Solid-State Lett. **2**, 607–609 (1999)

27. D.Q. Liu, X.Q. Liu, Z.Z. He, The elevated temperature performance of $LiMn_2O_4$ coated with $Li_4Ti_5O_{12}$ for lithium ion battery. Mater. Chem. Phys. **105**, 362–366 (2007)

28. A.B. Puthirath, B. John, C. Gouri, S. Jayalekshmi, Lithium doped polyaniline and its composites with $LiFePO_4$ and $LiMn_2O_4$-prospective cathode active materials for environment friendly and flexible Li-ion battery applications. RSC Adv. **5**, 69220–69228 (2015)

29. H. Xia, Z. Luo, J. Xie, Nanostructured $LiMn_2O_4$ and their composites as high-performance cathodes for lithium-ion batteries. Prog. Nat. Sci. Mater. Int. **22**, 572–584 (2012)

30. S.H. Wu, M.T. Yu, Preparation and characterization of o-$LiMnO_2$ cathode materials. J. Power Sources **165**, 660–665 (2007)

31. Y. Huang, R. Jiang, S.J. Bao et al., $LiMn_2O_{4-y}Br_y$ nanoparticles synthesized by a room temperature solid-state coordination method. Nanoscale Res. Lett. **4**, 353–358 (2009)

32. S.J. Bao, Y.Y. Liang, H.L. Li, Synthesis and electrochemical properties of $LiMn_2O_4$ by microwave-assisted sol-gel method. Mater. Lett. **59**, 3761–3765 (2005)

33. X. He, J. Li, Y. Cai et al., Preparation of spherical spinel $LiMn_2O_4$ cathode material for Li-ion batteries. Mater. Chem. Phys. **95**, 105–108 (2006)

34. H. Guo, W. He, Y. Lu, X. Zhang, Self-crosslinked polyaniline hydrogel electrodes for electrochemical energy storage. Carbon N Y **92**, 133–141 (2015)

35. H. Liang, J. Ni, L. Li, Bio-inspired engineering of Bi_2S_3-PPy yolk-shell composite for highly durable lithium and sodium storage. Nano Energy **33**, 213–220 (2017)

36. W. Li, F. Gao, X. Wang et al., Strong and robust polyaniline-based supramolecular hydrogels for flexible supercapacitors. Angew. Chem. Int. Ed. **55**, 9196–9201 (2016)

37. K. Li, J. Liu, Y. Huang et al., Integration of ultrathin graphene/polyaniline composite nanosheets with a robust 3D graphene framework for highly flexible all-solid-state supercapacitors with superior energy density and exceptional cycling stability. J. Mater. Chem. A **5**, 5466–5474 (2017)

38. R.K.L. Tan, S.P. Reeves, N. Hashemi et al., Graphene as a flexible electrode: review of fabrication approaches. J. Mater. Chem. A **5**, 17777–17803 (2017)

39. Y. Lu, W. He, T. Cao et al., Elastic, conductive, polymeric hydrogels and sponges. Sci. Rep. **4**, 1–8 (2014)

40. H. Li, J. Song, L. Wang et al., Flexible all-solid-state supercapacitors based on polyaniline orderly nanotubes array. Nanoscale **9**, 193–200 (2017)

41. J. Luo, W. Zhong, Y. Zou et al., Preparation of morphology-controllable polyaniline and polyaniline/graphene hydrogels for high performance binder-free supercapacitor electrodes. J. Power Sources **319**, 73–81 (2016)

42. Z.H. Chen, K.L. Huang, S.Q. Liu, H.Y. Wang, Preparation and characterization of spinel $LiMn_2O_4$ nanorods as lithium-ion battery cathodes. Trans. Nonferrous Met. Soc. China (English Ed) **20**, 2309–2313 (2010)

43. Z. Durmus, A. Baykal, H. Kavas, H. Szeri, Preparation and characterization of polyaniline (PANI)-Mn_3O_4 nanocomposite. Phys. B **406**, 1114–1120 (2011)

44. D.K. Mlsra, Evaluation of the complex permittivity of layered dielectric materials with the use of an open-ended coaxial line. Microw. Opt. Technol. Lett. **137**, 183–187 (1996)

45. D.H. Snydacker, M. Aykol, S. Kirklin, C. Wolverton, Lithium-ion cathode/coating pairs for transition metal containment. J. Electrochem. Soc. **163**, A2054–A2064 (2016)

46. Y. Kan, Y. Hu, C.K. Lin et al., Migration of Mn cations in delithiated lithium manganese oxides. Phys. Chem. Chem. Phys. **16**, 20697–20702 (2014)

47. N. Ahmed, M. Ramadan, W.M.A. El, Non-precious co-catalysts boost the performance of TiO_2 hierarchical hollow mesoporous spheres in solar fuel cells. Int. J. Hydrog. Energy **43**, 21219–21230 (2018)

48. P.A. Yadav, A.V. Deshmukh, K.P. Adhi et al., Role of grain size on the magnetic properties of $La_{0.7}Sr_{0.3}MnO_3$. J. Magn. Magn. Mater. **328**, 86–90 (2013)

49. B. Zhao, R. Ran, M. Liu, Z. Shao, A comprehensive review of $Li_4Ti_5O_{12}$-based electrodes for lithium-ion batteries: the latest advancements and future perspectives. Mater. Sci. Eng. R **98**, 1–71 (2015)

50. L.Y. Yang, H.Z. Li, J. Liu et al., $Li_4Ti_5O_{12}$ nanosheets as high-rate and long-life anode materials for sodium-ion batteries. J. Mater. Chem. A **3**, 24446–24452 (2015)

51. V.J. Babu, S. Vempati, S. Ramakrishna, Conducting polyaniline-electrical charge transportation. Mater. Sci. Appl. **4**, 1–10 (2013)

52. A.S. Roy, S.G. Hegde, A. Parveen, Synthesis, characterization, AC conductivity, and diode properties of polyaniline-

CaTiO$_3$ composites. Polym. Adv. Technol. **25**, 130–135 (2014)

53. S.M. Ebrahim, Fabrication of Schottky diode based on Zn electrode and polyaniline doped with 2-acrylamido-2-methyl-1-propanesulfonic acid sodium salt. J. Polym. Res. **16**, 481–487 (2009)

54. M. Khairy, M.A. Mousa, Influences of γ–radiation and surfactants on electrical and magnetic properties of Cu$_{0.1}$Zn$_{0.9}$Mn$_2$O$_4$ nanoparticles. Int. J. Mater. Chem. **2**, 197–204 (2013)

55. Z.Y. Yang, Y.F. Zhao, Q.Q. Xiao et al., Controllable growth of CNTs on graphene as high-performance electrode material for supercapacitors. ACS Appl. Mater. Interfaces **6**, 8497–8504 (2014)

56. L. Wang, Y. Ye, X. Lu et al., Hierarchical nanocomposites of polyaniline nanowire arrays on reduced graphene oxide sheets for supercapacitors. Sci. Rep. **3**, 1–9 (2013)

57. M. Ciszewski, A. Mianowski, P. Szatkowski et al., Reduced graphene oxide–bismuth oxide composite as electrode material for supercapacitors. Ionics (Kiel) **21**, 557–563 (2014)

58. P. Gellings, H. Bouwmeester, *The CRC handbook of solid state electrochemistry*, 1st edn. (CRC Press, Boca Raton, 1997)

59. M.A. Mousa, M. Khairy, M. Shehab, Nanostructured ferrite/graphene/polyaniline using for supercapacitor to enhance the capacitive behavior. J. Solid State Electrochem. **21**, 995–1005 (2017)